# Analysis of the Poisson–Nernst–Planck equation in a ball for modeling the Voltage–Current relation in neurobiological microdomains

J. Cartailler [b], Z. Schuss [c], D. Holcman [a,b,*]

[a] *Mathematical Institute, University of Oxford, Andrew Wiles Building, Woodstock Rd, Oxford OX2 6GG, United Kingdom*
[b] *Ecole Normale Supérieure, 46 rue d'Ulm 75005 Paris, France*
[c] *Department of Mathematics, Tel-Aviv University, Tel-Aviv 69978, Israel*

## HIGHLIGHTS

- Analysis of electrodiffusion using the Poisson–Nernst–Planck equations in a ball.
- Model of voltage changes under the non-electroneutrality assumption in a dendritic spine.
- Analysis and prediction of the Current–Voltage relation in a dendritic spine: role of the geometry in long-range interaction, beyond the Debye length.

## ARTICLE INFO

## ABSTRACT

The electro-diffusion of ions is often described by the Poisson–Nernst–Planck (PNP) equations, which couple nonlinearly the charge concentration and the electric potential. This model is used, among others, to describe the motion of ions in neuronal micro-compartments. It remains at this time an open question how to determine the relaxation and the steady state distribution of voltage when an initial charge of ions is injected into a domain bounded by an impermeable dielectric membrane. The purpose of this paper is to construct an asymptotic approximation to the solution of the stationary PNP equations in a $d$-dimensional ball ($d = 1, 2, 3$) in the limit of large total charge. In this geometry the PNP system reduces to the Liouville–Gelfand–Bratú (LGB) equation, with the difference that the boundary condition is Neumann, not Dirichlet, and there is a minus sign in the exponent of the exponential term. The entire boundary is impermeable to ions and the electric field satisfies the compatibility condition of Poisson's equation. These differences replace attraction by repulsion in the LGB equation, thus completely changing the solution. We find that the voltage is maximal in the center and decreases toward the boundary. We also find that the potential drop between the center and the surface increases logarithmically in the total number of charges and not linearly, as in classical capacitance theory. This logarithmic singularity is obtained for $d = 3$ from an asymptotic argument and cannot be derived from the analysis of the phase portrait. These results are used to derive the relation between the outward current and the voltage in a dendritic spine, which is idealized as a dielectric sphere connected smoothly to the nerve axon by a narrow neck. This is a fundamental microdomain involved in neuronal communication. We compute the escape rate of an ion from the steady density in a ball, which models a neuronal spine head, to a small absorbing window in the sphere. We predict that the current is defined by the narrow neck that is connected to the sphere by a small absorbing window, as suggested by the narrow escape theory, while voltage is controlled by the PNP equations independently of the neck.

© 2016 Elsevier B.V. All rights reserved.

## 1. Introduction

In this paper the PNP model [1] is used for the computation of the distribution in a ball of a single specie of unscreened positive charges in different regimes, including the limit of large total charge. The stationary PNP equations with Neumann and no-flux conditions, respectively, on the boundary of a bounded domain $\Omega$ reduce to Poisson's equation, which models the electrical potential, with an exponential term, which models the density of charges in $\Omega$ [2–7]. This system is also used to simulate the equilibration of ions between large reservoirs through narrow necks [2,8] and to study the effect of interacting ions in ionic channels [9].

* Correspondence to: Mathematical Institute, University of Oxford, Andrew Wiles Building, Woodstock Rd, Oxford OX2 6GG, United Kingdom.
*E-mail addresses:* schuss@post.tau.ac.il (Z. Schuss), david.holcman@ens.fr (D. Holcman).

We compute here the distribution of a single specie of un-screened positive charges in a ball for different regimes, including the limit of large charges. The stationary PNP equation with Neumann and no-flux conditions on the boundary of a bounded domain $\Omega$ is the classical Poisson equation with an exponential term, that model the electrical potential and density of charges in $\Omega$. This equation is also known as the Liouville–Gelfand–Bratú-type equation [10] for the electric potential with however two major differences: first, the boundary condition on $\partial\Omega$ is Neumann and not Dirichlet and second, there is a minus sign in the exponent, normalized over the domain $\Omega$. This question is thus different from the Newtonian potential of a cluster of self-gravitating mass distribution [11,12]. When the potential is attractive, as the mass tends to infinity, blow-up and concentration phenomena have been found and characterized [13–15]. This phenomenology is not expected to appear here due to the minus sign in front of the Laplacian. In addition, the PNP equation considered here should not be confused with the Poisson–Boltzmann equation, which is a model for two populations of negative and positive ions with the same valence charge. The aim of the present model is to investigate the consequence of the non-electro-neutrality assumption on the ionic charge interaction at large distances inside a confined domain.

We compute the solution of the stationary PNP equation in spherical symmetry in dimensions $\leq 3$ with respect to the (dimensionless) total charge $\lambda$. We construct asymptotic approximations of the solutions for small and large $\lambda$. The one-dimensional case is solved explicitly and it is characterized by a logarithmic singularity that develops in the large $\lambda$ limit at the boundary. The explicit solution in two-dimensions has a similar singularity on the boundary. The similar asymptotic behavior in three-dimensions cannot be computed explicitly, so we provide an asymptotic and numerical argument showing again that a logarithmic singularity develops at the boundary for large $\lambda$. We note that this singularity in three dimensions cannot be derived from the analysis of the phase portrait, because it occurs at the initial point of the phase-plane dynamics.

The present modeling and analysis is motivated by the need to compute voltage changes in bounded domains and to see how it develops a boundary layer for large $\lambda$. We find that the voltage change from the center to the boundary of the unit ball tends to infinity at a logarithmic rate as the total charge $\lambda$ increases to infinity. Finally, we apply this analysis to predict the voltage change (solution of the PNP equation) for idealized neuronal microdomains, such as dendritic spines under the non-electro-neutrality assumption. The biological structures (see Fig. 1) are idealized as a spherical dielectric membrane filled with ionic solution, connected to the dendrite by a cylindrical narrow neck. A large effort was dedicated to the study of the mathematics of diffusion in such structures [16,17], but very little is known about their electro-diffusion properties. This is the case even experimentally, where almost no data are available at the nanometer resolution (see [18–20]). This high resolution is necessary for the evaluation of the change in voltage and to determine whether or not there is electro-neutrality. Despite converging experimental efforts, the electrical properties of these structures remain unclear at a molecular level and a predictive theory, based on mathematical physics, is needed to interpret incoming data [21]. The PNP equations serve here to compute the electric field for a single specie, where we do not assume local electro-neutrality.

To derive a relation between the outward current and the voltage, we compute the escape rate of diffusing particles (ions) from the steady density in a ball to a small absorbing hole in its boundary, which is the window connecting it to the narrow neck. We find that the current of ions is controlled by the small absorbing window, as predicted by the narrow escape theory [22,23], while the voltage is independently regulated by the coupled PNP equations.
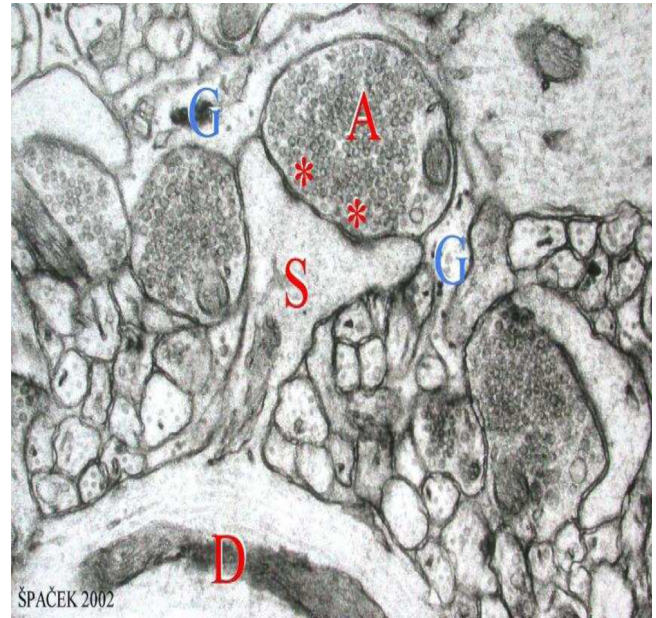


**Fig. 1.** Electron-microscopy image of a dendritic spine (courtesy of J. Spacek). Abbreviations G: glial cells, S: spine, D: dendrite, A: axon.
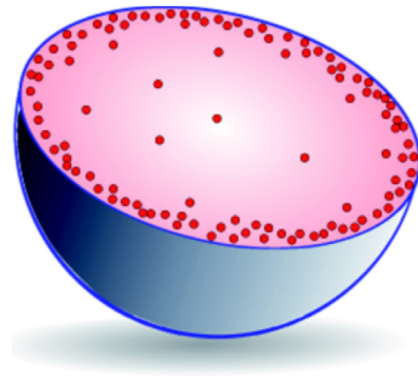


**Fig. 2.** Schematic representation of the distribution of a single unscreened ionic specie in a dielectric ball.

The paper is organized as follows. In the first part, we study the PNP equations asymptotically and numerically for a ball and demonstrate that charges accumulate at the boundary (see Fig. 2). In the second part, we estimate the current generated in an idealized dendritic spine that consists of a spherical head connected to the nerve axon by a narrow cylindrical neck. We calculate the efflux from the spine and demonstrate that the head geometry controls voltage, while the narrow neck radius controls the current.

## 2. PNP equations in a ball

We consider the Poisson–Nernst–Planck system in a ball $\Omega$ of radius $R$, whose dielectric boundary $\partial\Omega$ is represented as the compatibility condition for Poisson's equation and its impermeability to the passage of ions is represented as a no-flux boundary condition for the Nernst–Planck equation. We assume that there are $N$ positive ions of valence $z$ in $\Omega$ and that there is an initial particle density $q(\boldsymbol{x})$ in $\Omega$ such that

$$\int_{\Omega} q(\boldsymbol{x})\, d\boldsymbol{x} = N. \tag{1}$$

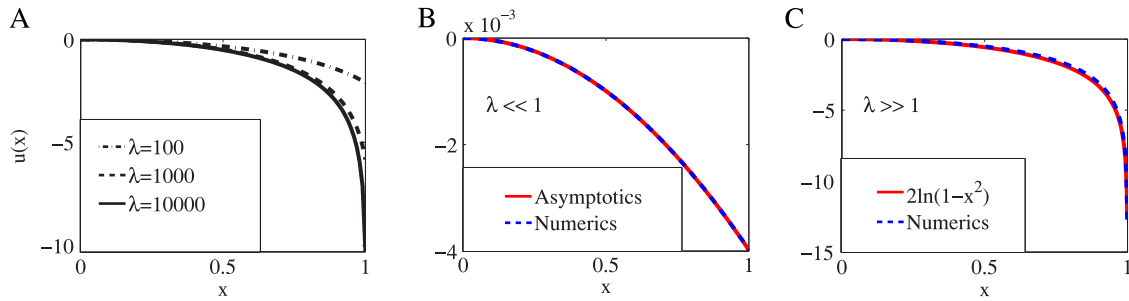The charge in $\Omega$ is

$$Q = zeN,$$

**Fig. 3.** Asymptotics behavior of the solution $u(x)$ for $d = 3$. (A) The profiles of $u(x)$ for the values $\lambda = 10^2, 10^3, 10^4$ of the parameter. (B, C) Two regimes are shown: for $\lambda = 0.1 \ll 1$, the approximation $u(x) = -\lambda x^2/8\pi + O(\lambda^2)$ (see (69)) and for $\lambda \gg 1$, where $u(x) \approx 2\log(1 - x^2)$. The analytical approximations (red) are compared with the numerical solutions (see Appendix A.4). (For interpretation of the references to color in this figure legend, the reader is referred to the web version of this article.)

where $e$ is the electronic charge. The charge density $\rho(\boldsymbol{x}, t)$ is the solution of the Nernst–Planck equation

$$D\left[\Delta\rho(\boldsymbol{x}, t) + \frac{ze}{kT}\nabla\left(\rho(\boldsymbol{x}, t)\nabla\phi(\boldsymbol{x}, t)\right)\right] = \frac{\partial\rho(\boldsymbol{x}, t)}{\partial t} \quad \text{for } \boldsymbol{x} \in \Omega \tag{2}$$

$$D\left[\frac{\partial\rho(\boldsymbol{x}, t)}{\partial n} + \frac{ze}{kT}\rho(\boldsymbol{x}, t)\frac{\partial\phi(\boldsymbol{x}, t)}{\partial n}\right] = 0 \quad \text{for } \boldsymbol{x} \in \partial\Omega \tag{3}$$

$$\rho(\boldsymbol{x}, 0) = q(\boldsymbol{x}) \quad \text{for } \boldsymbol{x} \in \Omega, \tag{4}$$

where $\phi(\boldsymbol{x}, t)$, the electric potential in $\Omega$, is the solution of the time-dependent Poisson equation (Gauss' law)

$$\Delta\phi(\boldsymbol{x}, t) = -\frac{ze\rho(\boldsymbol{x}, t)}{\varepsilon\varepsilon_0} \quad \text{for } \boldsymbol{x} \in \Omega \tag{5}$$

with the boundary condition

$$\frac{\partial\phi(\boldsymbol{x}, t)}{\partial n} = -\sigma(\boldsymbol{x}, t) \quad \text{for } \boldsymbol{x} \in \partial\Omega, \tag{6}$$

where $\sigma(\boldsymbol{x}, t)$ is the surface charge density on the boundary $\partial\Omega$. In the steady state and in spherical symmetry

$$\sigma(\boldsymbol{x}, t) = \frac{Q}{4\varepsilon\varepsilon_0\pi R^2}. \tag{7}$$

### 2.1. The steady-state solution

In the steady state, we get from (2) that the density is

$$\rho(\boldsymbol{x}) = N\frac{\exp\left\{-\frac{ze\phi(\boldsymbol{x})}{kT}\right\}}{\int_\Omega \exp\left\{-\frac{ze\phi(\boldsymbol{x})}{kT}\right\} d\boldsymbol{x}}, \tag{8}$$

hence (5) gives

$$\Delta\phi(\boldsymbol{x}) = -\frac{zeN\exp\left\{-\frac{ze\phi(\boldsymbol{x})}{kT}\right\}}{\varepsilon\varepsilon_0\int_\Omega \exp\left\{-\frac{ze\phi(\boldsymbol{x})}{kT}\right\} d\boldsymbol{x}}. \tag{9}$$

In spherical symmetry in $\mathbb{R}^d$, Eq. (9) can be written in spherical coordinates as

$$\phi''(r) + \frac{d-1}{r}\phi'(r) = -\frac{zeN\exp\left\{-\frac{ze\phi(r)}{kT}\right\}}{S_d\varepsilon\varepsilon_0\int_0^R \exp\left\{-\frac{ze\phi(r)}{kT}\right\} r^{d-1} dr} < 0, \tag{10}$$

where $S_d$ is the surface area of the unit sphere in $\mathbb{R}^d$. The boundary conditions are

$$\frac{\partial\phi(0)}{\partial r} = 0, \qquad \frac{\partial\phi(R)}{\partial r} = -\frac{Q}{\varepsilon\varepsilon_0 S_d R^{d-1}}. \tag{11}$$

The inequality in (10) means that $\phi(r)$ has a maximum at the origin and decreases toward the boundary (see Fig. 3(A)). The radius is non-dimensionalized by setting $r = Rx$ for $0 < x < 1$ and

$$u(x) = \frac{ze\phi(r)}{kT}, \qquad \lambda = \frac{(ze)^2 N}{\varepsilon\varepsilon_0 kT}, \tag{12}$$

to write (10) as the dimensionless equation

$$u''(x) + \frac{d-1}{x}u'(x) = -\frac{\lambda \exp\{-u(x)\}}{S_d R^{d-2}\int_0^1 \exp\{-u(x)\} x^{d-1}dx} \tag{13}$$

$$u(0) = 0, \qquad u'(0) = 0.$$

We can always assume $u(0) = 0$, because the solution is defined up to an additive constant for the Neumann boundary condition. This additional condition leads to the three boundary conditions: $u(0) = u'(0) = 0$ and the Neumann condition at the boundary. In this form the phase plane for (13) can be analyzed by the dynamical system approach and numerical solutions can be constructed by the shooting method. Note that the compatibility condition on the boundary at $x = 1$ has been dropped, because it is automatically satisfied by a solution. Incorporating the denominator of the right hand side of (13) into the parameter $\lambda$ by setting

$$\lambda = \mu S_d R^{d-2}\int_0^1 \exp\{-u(x)\} x^{d-1} dx, \tag{14}$$

we can write the initial value problem (13) as

$$u''(x) + \frac{d-1}{x}u'(x) = -\mu \exp\{-u(x)\} \tag{15}$$

$$u(0) = u'(0) = 0.$$

First, we show that solutions exist in dimensions $1 \le d \le 3$ only for $\mu$ in the range $0 \le \mu < \mu^*$ for some positive $\mu^*$ inside the interval $[0, 1]$. The key issue is, indeed, to determine the range of $\mu$, for which (15) has a solution that exists in the interval $0 < x \le 1$. Actually, it is shown below that there is a critical $\mu^*$ so that for $0 < \mu < \mu^*$, (15) has no singularities in the interval $0 < x < 1$. Thus the value $\mu^*$ is characterized by the condition that the singularity occurs at $x = 1$.

**The solution for $d = 1$**

In one dimension (15) is solved in Appendix A.1 as (see (52))

$$u_\lambda^{1D}(x) = \log\cos^2\sqrt{\frac{\lambda}{2I_\lambda}}x, \tag{16}$$

where $I_\lambda$ is solution of the implicit equation

$$I_\lambda = \frac{2}{\lambda}\tan^2\sqrt{\frac{\lambda}{2I_\lambda}}. \tag{17}$$
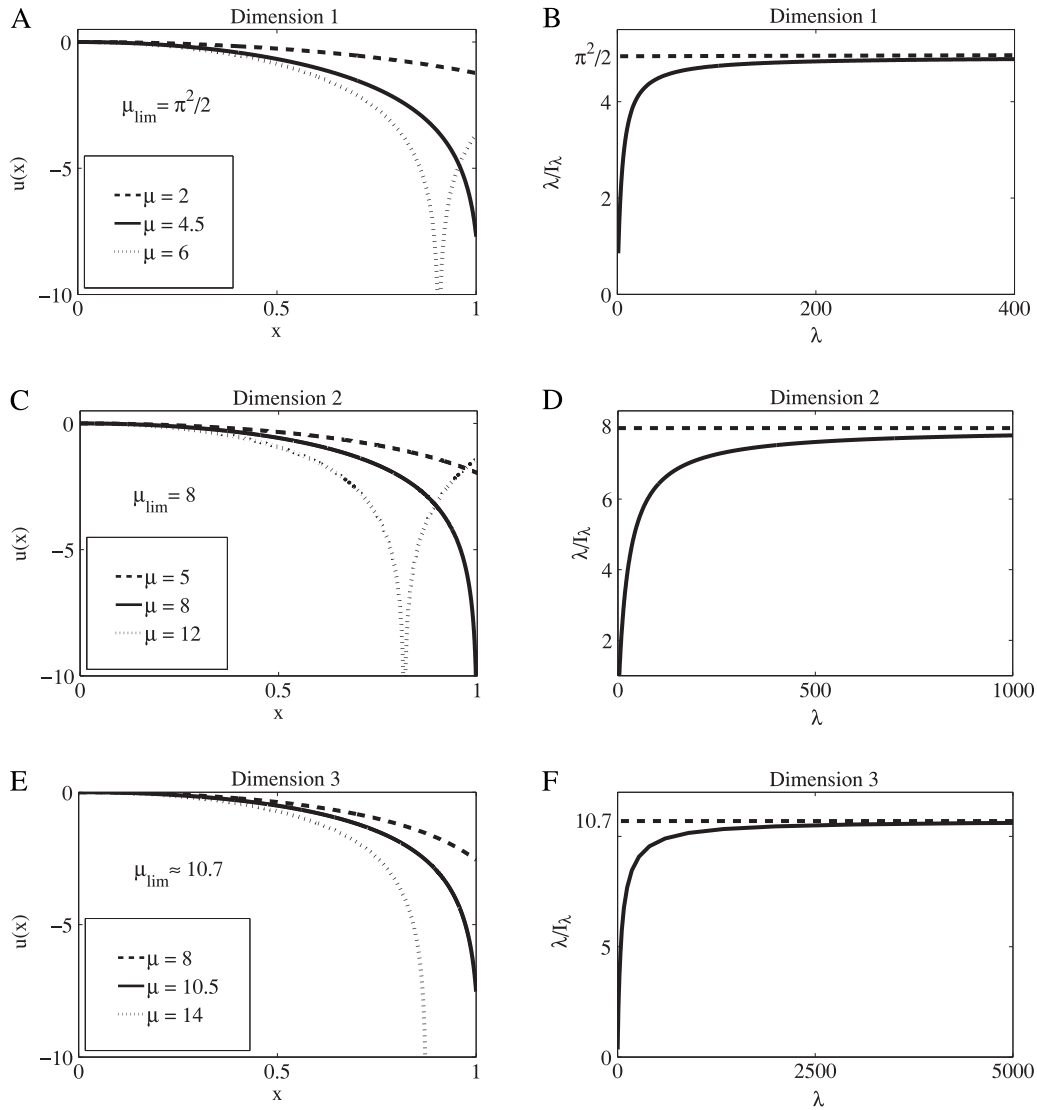
**Fig. 4.** Numerical solutions $u(x)$ of the initial value problem (15). (A), (C), and (E) correspond to different profile values of $\lambda$ in dimensions 1, 2, and 3, respectively. The dotted curves are solutions that blow-up for $x < 1$. (B), (D), and (F) are plots of the ratio $\lambda/I_\lambda$ for $d = 1, 2, 3$, respectively.

The graph of $u_\lambda^{1D}(x)$ is shown in Fig. 4(A), while the one for $\lambda/I_\lambda$ vs. $\lambda$ is shown in Fig. 4(B). Thus, according to (14),

$$0 < \mu(\lambda) = \frac{\lambda}{I_\lambda} \le \frac{\pi^2}{2}, \qquad \lim_{\lambda \to \infty} \mu(\lambda) = \frac{\pi^2}{2}.$$

Thus the solution $u_\lambda^{1D}$ exists for all $\lambda > 0$ and a logarithmic singularity develops at the boundary $x = 1$ in the limit $\lambda \to \infty$.

**The case $d = 2$**

The solution in the two-dimensional case is given in Appendix A.2 as

$$u_\lambda^{2D}(x) = \log\left(1 - \frac{\lambda}{8I_\lambda} x^2\right)^2,$$

where

$$I_\lambda = \pi + \frac{\lambda}{8}, \qquad \mu(\lambda) = \frac{\lambda}{I_\lambda}, \qquad \lim_{\lambda \to \infty} \mu(\lambda) = 8.$$

The graph of $u_\lambda^{2D}(x)$ is shown in Fig. 4(C), while the one for $\lambda/I_\lambda$ is in Fig. 4(D). The solution $u_\lambda^{2D}(x) = \log\left(1 - \frac{\lambda x^2}{\lambda+8\pi}\right)^2$ develops a logarithmic singularity in the limit $\lambda \to \infty$.

**The case $d = 3$**

The solution of the initial value problem (15) in three dimensions cannot be computed explicitly. The solution exists for all $\lambda$, while there is a critical value $\mu^*$, above which there is no regular solution. Unlike the cases $d = 1, 2$, the value of $\mu^*$ can only be estimated numerically. Indeed, phase-plane analysis shows that the solution of (15) is unique when it exists. However, it is not possible to use the phase-plane for the study of the singularity of the solution, because it occurs at the initial point of the phase-plane dynamics. To study the asymptotic explosion of the solution, an asymptotic approximation is needed. The solution is constructed numerically (see Appendix A.4 for the construction of a numerical scheme).

Next, we show that the problem (13) has a unique regular solution for all $\lambda \ge 0$, when the solution is finite. The proof of uniqueness of the solution follows the phase-plane analysis of (15). Indeed, changing the variables to [24]

$$s = -\log r, \qquad u(r) = U(s), \qquad v(s) = \frac{dU(s)}{ds},$$

$$w = \mu e^{-2s} e^{-U(s)}$$

$$w'(s) = -2w(s) - U'(s)w(s) = w(s)[2 - v(s)], \qquad (18)$$

the phase-plane dynamics of (15) becomes

$$v'(s) = v(s) - w(s),$$
$$w'(s) = -w(s)[2 + v(s)], \tag{19}$$

and can be written as the first-order ODE

$$\frac{dw}{dv} = \frac{-w(2+v)}{v-w}. \tag{20}$$

The phase plane of (19) contains exactly two critical points, the origin **0**, which is a saddle point and the line $w = 3v$ is the tangent **T** to its stable manifold, and the point $P_a = (-2, -2)$, which is an unstable node. The initial conditions $u(0) = u'(0) = 0$ for the solution of (15) impose $\lim_{s\to\infty} U(s) = u(0) = 0$ and $\lim_{s\to\infty} U'(s) = -\lim_{r\to 0} ru'(r) = v(0) = 0$, hence the constraints

$$\lim_{s\to\infty} v(s) = 0, \qquad \lim_{s\to\infty} w(s) = \lim_{s\to\infty} \mu e^{-2s}e^{-U(s)} = 0. \tag{21}$$

Thus the trajectory of the solution of (15) in the first quadrant, which satisfies the constraints (21), has to be on the separatrix that converges to the saddle point. Choosing any value $U(0)$ gives $\mu e^{-U(0)}$ the value of $v(0) = U'(0)$, which has to be chosen on the separatrix. Therefore, starting in the first quadrant, a trajectory of (19) converges to the saddle point if and only if it starts on the separatrix with the tangent **T**. The stable branch at the saddle point tends to infinity as $s \downarrow 0$. Indeed, the local expansion of (20) near the saddle point is

$$w(v) = 3v + \frac{3}{5}v^2 - \frac{3}{175}v^3 + \cdots, \tag{22}$$

which gives the phase portrait shown in Fig. 5. Along the separatrix $w'(v) > 0$, except at the origin, showing that there is a unique solution for an initial value $v(0)$. However, phase-space analysis of the singular solution is impossible, because the singularity occurs at the initial point and thus the Cauchy problem is undefined. It follows that the problem (13) has a finite solution and the phase diagram plotted in Fig. 5 ensures that for any finite initial condition $(v(0), w(0))$ on the separatrix in the first quadrant there is a unique solution to (19) that satisfies (21).

A numerical solution of (13) gives the graph Fig. 3(E), which is the solution $u(x)$ of (3) for $\mu \leq \mu^* = 11.2$. The graph in dashed line ($\mu^* = 14$) blows up before reaching $x = 1$, while the dotted line is finite throughout the interval. To estimate an upper bound for $\mu^*$, note that whenever the solution exists for some $\mu$ near $\mu^*$, its asymptotic behavior for $x$ close to 1 shows that $u''(1) \gg u'(1)$ (see the blue line in Fig. 3). Indeed, to show that under the assumption $u''(1) \gg u'(1)$ the latter inequality is self-consistent, we note that the solution of (15) near $x = 1$ can be approximated by the solution of the simpler problem

$$\tilde{u}''(x) = -\mu \exp\left\{-\tilde{u}(x)\right\}, \tag{23}$$

given by

$$\tilde{u}(x) \sim \log \cos^2 \sqrt{\frac{\mu}{2}} x. \tag{24}$$

Thus $\tilde{u}(x)$ is finite in the interval as long as

$$\mu < \frac{\pi^2}{2} = 4.934802202 = \mu^* \tag{25}$$

and

$$\frac{\tilde{u}'(x)}{\tilde{u}''(x)} \leq \frac{|\sqrt{\mu} - \sqrt{\mu^*}|}{\sqrt{\mu^*}} \ll 1. \tag{26}$$

Thus it follows at this stage that there are solutions for fixed values of $\mu$ below and above $\mu^*$, where above $\mu^*$ they blow up inside the
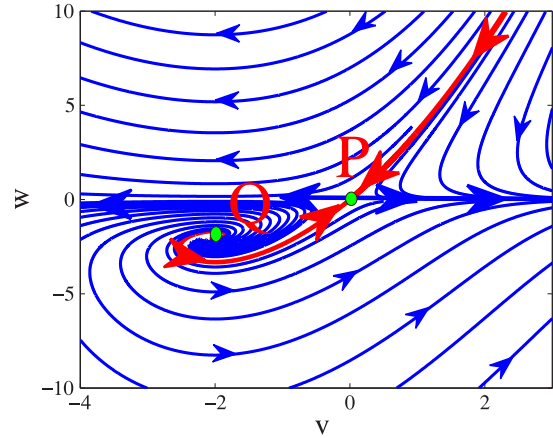


**Fig. 5.** The phase-plane of (19). The separatrix is shown in red, while the other trajectories are in blue. (For interpretation of the references to color in this figure legend, the reader is referred to the web version of this article.)
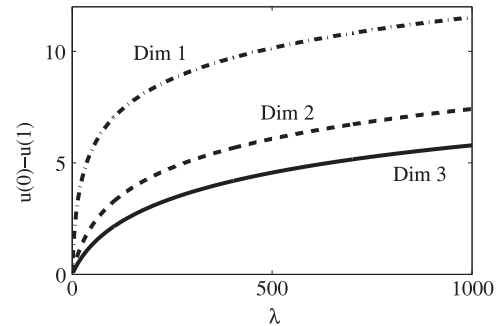


**Fig. 6.** Asymptotics of $u_\lambda(1) - u_\lambda(0)$ for dimensions 1,2 and 3.

interval $0 < x < 1$ (frames A, C, E of Fig. 4). When $\mu$ varies with $\lambda$ according to (14), the solutions exist for all values of $\lambda$ (frames B, D, F of Fig. 4). The potential drop between the center and the surface of the sphere as a function of $\lambda$ is shown in Fig. 4(A)–(C)–(E) for $1 \leq d \leq 3$.

In Fig. 3, the three-dimensional solutions obtained numerically, are compared with the asymptotic expansions in two regimes. Appendix A.3 shows the expansion $u(x) = -\lambda\frac{x^2}{8\pi} + O(\lambda^2)$ for $\lambda \ll 1$ (see (69)). In contrast, for $\lambda \gg 1$, as mentioned above, the approximation $u(x) \approx 2\log(1 - x^2)$, which is valid near $x = 1$, can be used in the entire domain [0, 1]. The analytical approximations (red) are compared with the numerical solutions (see Appendix A.4).

**The potential drop**

The difference $u(0) - u(1)$ a physical meaning, as it represents the difference of potential drop the center and the boundary of a sphere. For $d = 1$,

$$|u_\lambda(1) - u_\lambda(0)| = \log\cos^2\sqrt{\frac{\lambda}{2I_\lambda}}, \tag{27}$$

where $\lambda/2I_\lambda \to \pi^2/4$ as $\lambda \to \infty$. For $d = 2$,

$$|u_\lambda(1) - u_\lambda(0)| = 2\log\left(\frac{8\pi}{\lambda + 8\pi}\right), \tag{28}$$

and for $d = 3$ and $\lambda \gg 1$,

$$|u_\lambda(1) - u_\lambda(0)| = 2\log[1 - f(\lambda)], \tag{29}$$

where the unknown function $f$ is increasing and $f(\lambda) \to 1$ as $\lambda \to \infty$. The different curves for $d = 1, 2, 3$ are shown in Fig. 6. In all cases, the large $\lambda$ asymptotics behave logarithmically.
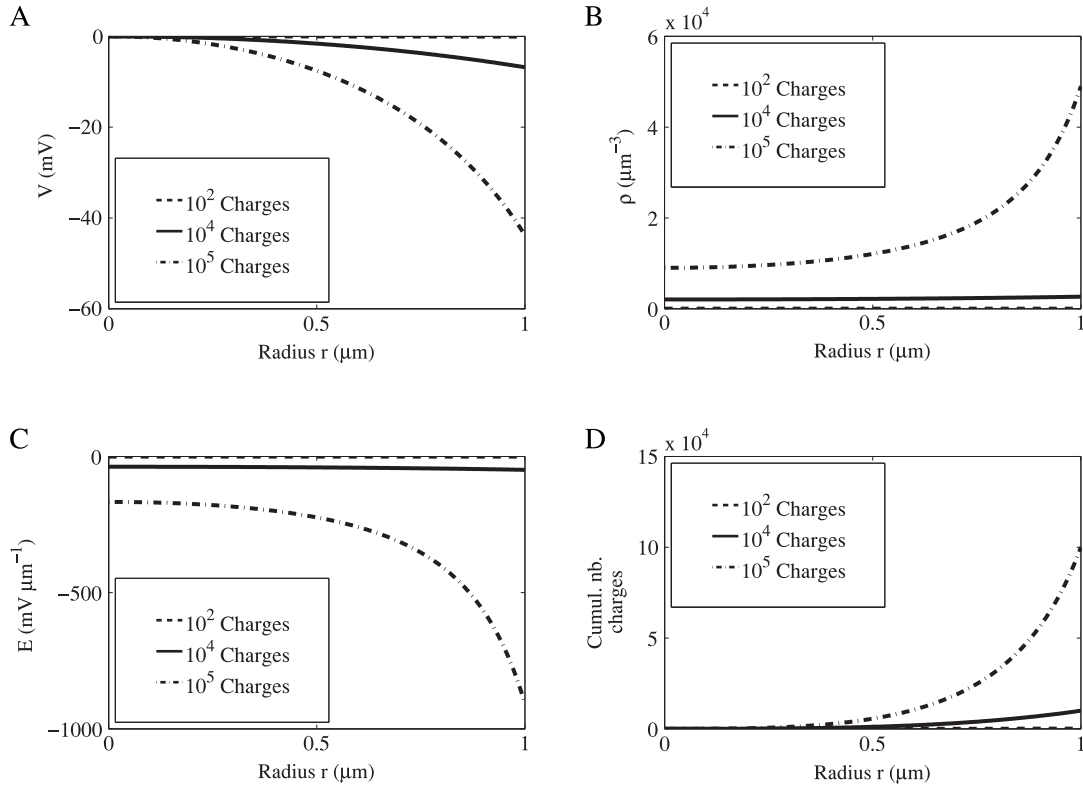
A



B



C



D



**Fig. 7.** Distribution of (A) the potential, (B) charge and the field (C) and cumulative density of charges (D) inside a dielectric ball. Parameters of simulations are given in Table 1.

**Table 1**
Parameters.

| Parameter | Description | Value |
|---|---|---|
| $z$ | Valence of ion | $z = 1$ (for sodium) |
| $D$ | Diffusion coefficient | $D = 200\ \mu m^2/s$ |
| $I_c$ | Injected current | $I \in [2; 30]$ pA |
| $I$ | Average Injected current | $I = 2.5$ pA |
| $\Omega$ | Spine head | $\Omega$ (volume $|\Omega| = 1\ \mu m^3$) |
| $a$ | Radius of spine neck | (typical) $a = 0.1\ \mu m$ |
| $L$ | Length of spine | (typical) $L = 1\ \mu m$ |
| $T$ | Temperature | $T = 300$ K |
| $E$ | Energy | $kT = 2.58 \times 10^{-2}$ eV |
| $e$ | Electron charge | $e = 1.6 \times 10^{-19}$ C |
| $\varepsilon$ | Dielectric constant | $\varepsilon = 80$ |

### 2.2. Physical implications of voltage and charge distributions in a dielectric ball

The distribution of voltage and charge in a dielectric ball can be estimated from the results of the previous sections by using the dimensional relation (12) in a ball of radius $R = 1\ \mu m$. Fig. 7(A) shows the voltage drop for $N = 10^2$, $10^3$ and $10^4$ charges. Already for 1000 charges, there is a difference between the center and the surface of a ball of few millivolts. Moreover, the density of charge is concentrated at the boundary (Fig. 7(B)), thus leading to a large field $E = -\nabla V$ close to the boundary (Fig. 7(C)). Consequently most of the charges are accumulated at the boundary, as revealed by the plot of the cumulative density of charges (Fig. 7(D))

$$Q(r) = N \frac{\int_0^r \exp\left\{-\frac{ze\phi(r)}{kT}\right\} r^2\, dr}{\int_0^R \exp\left\{-\frac{ze\phi(r)}{kT}\right\} r^2\, dr}. \tag{30}$$

In summary, when the total number of charges is fixed sufficiently high, the charges accumulate at the surface. The field is only significant close to the surface and thus can trap a Brownian charged particle in such a region, while outside a thin boundary layer the field is almost zero and charged particles experience no drift. This effect is discussed in the next section.

### 2.3. Scaling laws for the maximum number of charges

Although, as shown above, for a fixed radius the difference of potential $V(0) - V(1)$ is bounded as a function of the total number of charges, the maximal number of charges increases linearly with the radius of the ball, as shown below. Indeed, introducing the dimensionless radial variable $\zeta = r/R$ and setting $u_\lambda(r) = U_{\lambda/R}(\zeta)$, Eq. (10) becomes

$$U''_{\lambda/R}(\zeta) + \frac{2}{\zeta} U'_{\lambda/R}(\zeta) = -\frac{\lambda \exp\left\{-U_{\lambda/R}(\zeta)\right\}}{4\pi R \int_0^1 \exp\left\{-U_{\lambda/R}(\zeta)\right\}\ \zeta^2\, d\zeta}, \tag{31}$$

with the initial conditions $U_{\lambda/R}(0) = U'_{\lambda/R}(0) = 0$. The solution of the initial value problem

$$V''_\mu(\zeta) + \frac{2}{\zeta} V'_\mu(\zeta) = -\mu \exp\left\{-V_\mu(\zeta)\right\}, \qquad V_\mu(0) = V'_\mu(0) = 0$$
$$W'_\mu(\zeta) = \zeta^2 \exp\left\{-V_\mu(\zeta)\right\}, \qquad W_\mu(0) = 0 \tag{32}$$

gives

$$u_\lambda(r) = V_\mu\left(\frac{r}{R}\right), \qquad \lambda = 4\pi \mu R W(1). \tag{33}$$

Thus the number of charges $Q$ in a ball or radius $R$ creates the same distribution as a charge $Q/R$ in a ball of radius one, which can be expressed as

$$Q(R) = RQ(1). \tag{34}$$

## 3. Ionic flux in a small absorbing window in a highly charged sphere

Distributing a large charge close to the boundary has various consequences. The first one concerns the mean first passage time (MFPT) $\bar{\tau}(\boldsymbol{x})$ from $\boldsymbol{x} \in \Omega$ to a small absorbing window $\partial \Omega_a$. The MFPT is the solution of the Pontryagin–Andronov–Vitt (PAV) boundary value problem [25],

$$D\left[\Delta \bar{\tau}(\boldsymbol{x}) - \frac{ze}{kT}\nabla \bar{\tau}(\boldsymbol{x}) \cdot \nabla \phi(\boldsymbol{x})\right] = -1 \quad \text{for } \boldsymbol{x} \in \Omega \tag{35}$$

$$\frac{\partial \bar{\tau}(\boldsymbol{x})}{\partial n} = 0 \quad \text{for } \boldsymbol{x} \in \partial \Omega_r \tag{36}$$

$$\bar{\tau}(\boldsymbol{x}) = 0 \quad \text{for } \boldsymbol{x} \in \partial \Omega_a, \tag{37}$$

where $\partial \Omega_a$ represents the small absorbing window and $\partial \Omega_r = \partial \Omega \setminus \partial \Omega_a$. Consider the case of a large field $|\nabla \phi(\boldsymbol{x})| \gg 1$ near the boundary $|\boldsymbol{x}| = 1$. The profile of $\phi(\boldsymbol{x})$ was studied in Section 2.1 (see Fig. 7). To study the solution of the PAV problem (35)–(37), a narrow neighborhood of $\partial \Omega_a$ is mapped smoothly into the upper half plane with coordinates $\boldsymbol{X} = (x, y, z)$, where $z = 0$ is the image of the boundary, $\tilde{\tau}(\boldsymbol{X}) = \bar{\tau}(\boldsymbol{x})$, and outside a boundary layer near $\partial \Omega_a$

$$V = \frac{\partial \phi(\boldsymbol{x})}{\partial n}\bigg|_{|\boldsymbol{x}|=1} = const, \qquad \Phi(x, y) = \phi(\boldsymbol{x})\bigg|_{|\boldsymbol{x}|=1} = const,$$

so that $\nabla_{x,y} \Phi(x, y) = 0$. The PAV system (35)–(37) is converted to

$$\tilde{\tau}_{zz}(\boldsymbol{X}) - \frac{ze}{kT}\tilde{V}\tilde{\tau}_z(\boldsymbol{X}) + \Delta_{x,y}\tilde{\tau}(\boldsymbol{X}) = -\frac{1}{D}. \tag{38}$$

A regular expansion of $\tilde{\tau}(\boldsymbol{X})$ for large $\tilde{V} = \frac{\partial \phi}{\partial z}$ gives that to leading order $\tilde{\tau}(\boldsymbol{X})$ is a function of $(x, y)$ and setting $T(x, y) = \tilde{\tau}(x, y, 0)$, we find that

$$\Delta_{x,y} T(x, y) = -\frac{1}{D}. \tag{39}$$

Thus the MFPT from $\boldsymbol{x} \in \Omega$ to $\partial \Omega_a$ is the sum of the MFPT from $\boldsymbol{x}$ to $\partial \Omega$ and the MFPT form $\partial \Omega$ to $\partial \Omega_a$ on the surface $\partial \Omega$ (see [25]). The MFPT to $\partial \Omega$ is negligible relative to that to $\partial \Omega_a$. This approximation means that to reach $\partial \Omega_a$ in a highly charged ball, a charge entering through a channel would have the following statistical properties: a typical trajectory would be confined inside the boundary layer near the cell surface and thus the ion will move along the boundary. The field creates a large potential barrier near the reflecting part $\partial \Omega_r$ of the sphere with overwhelming probability. The ion could then find the target $\partial \Omega_a$ by an almost surface diffusion. A similar situation was already discussed in the context of confined of vesicles near a cell surface by a network of microtubules [26]. There are possible rare events that ions escape the boundary layer toward the center of the ball, where the field vanishes. This situation is, however, exceptional and the associated trajectories do not contribute much to the MFPT.

### 3.1. Particle current through a small absorbing window in a highly charged ball

A second consequence of the charge distribution is the control by the geometry of efflux of particles through a small hole. This has an important consequence in understanding how the electric voltage and current can be controlled in cellular microdomains such as dendritic spines (see the dictionary Appendix B). Diffusion in dendritic spines has already been investigated [27,28], but little is known about the regulation of the electrical current, because no experimental data are yet available about the voltage at a nanometer precision [21].

The present modeling and asymptotic analysis can lead to new predictions about the electrical current in a dendritic spine, which can be regulated independently of the voltage. This section focuses on the spine head. The solution $T(x, y)$ of (39) is the MFPT of Brownian motion on a sphere of radius $R$ to an absorbing circle centered at the north–south axis near the south pole, with small radius $a = R \sin\frac{\delta}{2}$. It is given by [17,29,30]

$$T(x, y) = \frac{2R^2}{D} \log \frac{\sin\frac{\theta}{2}}{\sin\frac{\delta}{2}}, \tag{40}$$

where $D$ is the diffusion coefficient, $\theta$ is the angle between $\boldsymbol{x}$ and the north pole. Thus

$$\bar{\tau}(\boldsymbol{x}) = T(x, y). \tag{41}$$

The MFPT, averaged over the sphere with respect to a uniform distribution of $\boldsymbol{x}$, is given by

$$\bar{\tau} = 2R^2 \left(\log \frac{1}{\delta} + O(1)\right) \quad \text{for } \delta \ll 1. \tag{42}$$

The MFPT for $N$ independent charges is

$$\bar{\tau}_N = \frac{2R^2}{N} \left(\log \frac{1}{\delta} + O(1)\right) \quad \text{for } \delta \ll 1. \tag{43}$$

It follows that the electrical current through the small window is given by

$$J = \frac{ze}{\bar{\tau}_N} = \frac{QD}{2R^2 \left(\log \frac{R}{a} + O(1)\right)} \quad \text{for } a \ll R. \tag{44}$$

The ball represents here the dendritic spine head and $J$ is the current through the neck. Thus, once a current flows into a dielectrics ball such as a spine head, the excess of charges $Q$ is first pushed toward the boundary, before moving by Brownian motion to the entrance of spine neck (small disk of size $a$). This result shows that the current $J$ in a spine head is governed by the spine geometry (see (44)) and a key parameter is the radius $a$ of the neck.

When there is no leak of charge, the current through the end of cylinder starting at the window (spine neck) and ending at a bigger cylinder (dendritic shaft) is the same as the one exiting the spine head. Under these conditions, the spine neck length neither affects nor modulates the current.

## 4. Discussion and applications of PNP to the current in a spine neck under voltage-clamp conditions

The PNP equations serve here as a model for the study of the current in neuronal microdomains, such as dendritic spines. The present analysis of the PNP equations can be used to estimate the voltage changes in dendritic spines when the voltage is maintained in the spine head. The one-charge model allows exploring the consequence of non-electro-neutrality at large distances (compared to the Debye length). It is found here that the voltage $U$ varies nonlinearly with respect to the total number of charges $Q$, unlike in the classical law of electrostatics for a conductor, where $Q = CU$ and $C$ is the capacitance.

Recall that a certain fraction of dendritic spines are interconnected, which is essential for neuronal communication [21]. Although the functions of the interconnections are still unclear, they are involved in regulating synaptic transmission and plasticity [18–20,31–33]. Interestingly, most of the excitatory connections occur not on the dendrite but rather on spines and the reason is still not clear. The spine shape is quite intriguing, made of a head connected to the dendritic shaft by a cylinder. We found here that this geometry plays a key role: this paper predicts that the spine head geometry determines the drop of voltage, while the current

is defined by the diffusion on the surface and the mean time of a two-dimensional Brownian motion to find the entrance to the neck (see [22,23]).

Under voltage-clamp conditions in the neck (the voltage is maintained constant), when a constant voltage difference between the head and the neck is imposed, the voltage–current relation follows a resistance law. Thus the spine geometry defines both the capacitance and resistance in geometrical terms, a vision that complements previous traditional studies [32,34,35].

Determining the voltage drop between the membrane of the spine head and the dendrite, when a current is flowing from the head to the dendrite, remains challenging, because the classical cable theory cannot be applied in a system that cannot be approximated by a cable. The general scheme for modeling the electro-diffusion in the spine is the PNP model in the head and a one-dimensional conduction of ions in the neck. The neck is considered a classical ionic conductor. Thus the steady-state PNP equations have to be solved in the sphere with boundary conditions implied by the compatibility condition and the flux through the neck is determined by the mean first passage time (MFPT) of ions from the head to the neck, as discussed above.

In the case of high charge $Q$ the potential turns out to be practically flat throughout the ball with a sharp boundary layer with negative slope at the boundary. Thus a charge diffuses and is pushed strongly toward the membrane so ionic motion is practically confined to motion on the surface. Due to spherical symmetry, the potential is constant on the boundary so ionic motion is free Brownian motion on a sphere. At high charge ions interact through the ambient potential that is determined from Poisson's equation in the ball. Therefore they can be assumed independent free Brownian particles. The MFPT $\bar{\tau}$ of an ion to the narrow opening of the neck is determined from the two-dimensional NET theory (see previous section and also [26] for a similar question where a three-dimensional search is reduced to a two-dimensional one for vesicles moving inside the cell cytoplasm). Because the flux carried by a single ion is $q/\bar{\tau}$, where $q$ is the ionic charge, the number of ions in the spine head is $N = Q/q$ and the MFPT $\bar{\tau}_N$ of any of the $N$ ions is given by

$$\bar{\tau}_N = \frac{\bar{\tau}}{N}. \tag{45}$$

Thus the current through the neck is

$$I = \frac{Q}{\bar{\tau}} \tag{46}$$

and due to charge conservation, it is independent of the length of the neck. If we consider the neck to be a parallel-plate capacitor carrying a steady current $I$, then the voltage drop across the neck is simply $V = RI$, where $R$ is the resistance of the neck, given by

$$R = \frac{kTL^2}{q^2 nD}, \tag{47}$$

where $k$ is Boltzmann's constant, $T$ is absolute temperature, $L$ is the length of the conductor, $n$ is the number of ions in the neck, $q$ is the charge of an ion, and $D$ is the diffusion coefficient of the solution in the neck [25]. This model is valid as along as the voltage is maintained in the spine head.

Finally, computing in the transient regime, the change in voltage drop between the spine head and the dendritic shaft, requires solving the time-dependent PNP equations. Another open question is to study the influence of the spine head geometry on the distribution of charges. Computing the distribution of charges and the associated field in non-convex geometry is certainly the most challenging.

## Appendix A

In this appendix, we first solve analytically the LGB equation (13) in dimensions one and two and in the second part, we describe the numerical methods to compute the solution in dimension 3.

### A.1. Solution of the minus sign LGB equation in the unit segment

The Cauchy problem for the LGB equation in the interval [01] is

$$-u_\lambda''(r) = \lambda \frac{e^{-u_\lambda(r)}}{\int_0^1 e^{-u_\lambda(r)} dr} \tag{48}$$

with the initial conditions

$$u_\lambda(0) = 0, \qquad u_\lambda'(0) = 0. \tag{49}$$

After a direct integration we get with the initial conditions (49)

$$u_\lambda'^2(r) = \frac{2\lambda}{I_\lambda}(e^{-u_\lambda(r)} - 1), \tag{50}$$

where

$$I_\lambda = \int_0^1 e^{-u_\lambda(r)} dr. \tag{51}$$

A second integration gives

$$u_\lambda(r) = \log \cos^2 \sqrt{\frac{\lambda}{2I_\lambda}} r. \tag{52}$$

Now we self-consistently calculate

$$I_\lambda = \int_0^1 e^{-u_\lambda(r)} dr = \int_0^1 \frac{dr}{\cos^2 \sqrt{\frac{\lambda}{2I_\lambda}} r} = \frac{1}{\sqrt{\frac{\lambda}{2I_\lambda}}} \tan \sqrt{\frac{\lambda}{2I_\lambda}}. \tag{53}$$

Thus $I_\lambda > 0$ is the solution of the implicit equation

$$I_\lambda = \frac{2}{\lambda} \tan^2 \sqrt{\frac{\lambda}{2I_\lambda}}. \tag{54}$$

The graph of $\lambda/I_\lambda$ versus $\lambda$ is shown in Fig. 4. We have $\lim_{\lambda\to\infty} \lambda/I_\lambda = \pi^2/2$, and specifically,

$$y_\lambda = \sqrt{\frac{\lambda}{2I_\lambda}} = \frac{\pi}{2} - \frac{\pi^2}{\lambda^2} + O\left(\frac{1}{\lambda^2}\right).$$

The solution (52) is shown in Fig. 4 and is regular in the entire interval $0 < r < 1$ for all values of $\lambda$. The drop between the extreme points of the interval is

$$u_\lambda(0) - u_\lambda(1) = \log \cos^2 \sqrt{\frac{\lambda}{2I_\lambda}} \tag{55}$$

and becomes infinite as the total charge increases indefinitely.

### A.2. The LGB equation for $d = 2$

The two-dimensional case can be transformed into the one dimensional case [24] by change of variable

$$r = e^{-t}, \quad \tilde{u}(t) = u_\lambda(r) - 2t.$$

Eq. (13) reduces to

$$-\tilde{u}_{tt}(t) = \frac{\lambda}{I_\lambda} e^{-\tilde{u}(t)+2t}, \tag{56}$$

where $I_\lambda = 2\pi \int_0^1 e^{-u_\lambda(r)} r\,dr$ and $w(t) = \tilde{u}(t) + 2t$ satisfies the equation

$$-w_{tt}(t) = \lambda \frac{e^{-w(t)}}{I_\lambda}. \tag{57}$$

The initial conditions are now transform to asymptotic conditions at infinity:

$$\lim_{t\to\infty}(w(t) - 2t) = 0, \qquad \lim_{t\to\infty}(\dot{w}(t) - 2)\,e^t = 0.$$

A first integration gives

$$\frac{\dot{w}^2(t)}{2} = \lambda \frac{e^{-w(t)}}{I_\lambda} + 2. \tag{58}$$

The solution is

$$w(t) = -\log\left(\frac{8}{(\lambda e^{2C+2t} - 1)^2}\right) - 2C - 2t, \tag{59}$$

where $C$ is a constant. Finally, we obtain that

$$u_\lambda(r) = \log\left(1 - \frac{\lambda r^2}{8 I_\lambda}\right)^2. \tag{60}$$

The integral

$$I_\lambda = \int_0^1 e^{-u_\lambda(r)} 2\pi r\,dr = \int_0^1 \frac{1}{\left(1 - \frac{\lambda}{8 I_\lambda} r^2\right)^2} 2\pi r\,dr$$

$$= \frac{8\pi}{8 - \lambda/I_\lambda} \tag{61}$$

gives

$$I_\lambda = \pi + \frac{\lambda}{8}, \qquad \lim_{\lambda\to\infty}\frac{\lambda}{I_\lambda} = 8. \tag{62}$$

The curve $\lambda/I_\lambda$ vs $\lambda$ is shown in Fig. 4 and $|u_\lambda(1) - u_\lambda(0)|$ in Fig. 6. Finally,

$$u_\lambda(r) = \log\left(1 - \frac{\lambda r^2}{\lambda + 8\pi}\right)^2,$$

$$|u_\lambda(1) - u_\lambda(0)| = 2\log\left(1 - \frac{\lambda}{\lambda + 8\pi}\right).$$

It follows that $u_\lambda(r)$ decreases smoothly and in the limit $\lambda \to \infty$, the solution blows-up over the entire boundary.

### A.3. Expansion of the solution of (15) for $\lambda \ll 1$

The regular expansion

$$u(\boldsymbol{x}) = u_0(\boldsymbol{x}) + \lambda u_1(\boldsymbol{x}) + \lambda^2 u_2(\boldsymbol{x}) + o(\lambda^2), \tag{63}$$

and (15) give that $u_0(\boldsymbol{x}) = 0$ and $u_1(\boldsymbol{x})$ is solution of

$$-\Delta u_1(\boldsymbol{x}) = \frac{1}{|\Omega|} \quad \text{on } \Omega \tag{64}$$

$$\frac{\partial u_1}{\partial \boldsymbol{n}} = -\frac{1}{|\partial\Omega|} \quad \text{on } \partial\Omega. \tag{65}$$

For $R = 1$,

$$u_1(r) = -\frac{r^2}{8\pi}, \tag{66}$$

with $u_1(0) = 0$. We conclude that $u_1(r) \leq 0$, Thus,

$$u(r) = -\frac{\lambda r^2}{8\pi} + O(\lambda^2). \tag{67}$$

The second order term $u_2$ is solution of

$$-\Delta u_2 = -\frac{u_1}{|\Omega|} \quad \text{on } \Omega, \tag{68}$$

with $u_2(0) = 0$ and $u_2'(0) = 0$. For $R = 1$,

$$u_2(r) = -\frac{3r^4}{640\pi^2}. \tag{69}$$

Thus,

$$u(r) = -\frac{\lambda r^2}{8\pi} - \frac{3\lambda^2 r^4}{640\pi^2} + O(\lambda^3). \tag{70}$$

### A.4. Numerical scheme for construction the solution of (13)

The solution $u(r)$ of (13) in previous sections was computed numerically by the one of the radial Neumann problem solvers in the ball $B_3$

$$v''(r) - \frac{2}{r}v'(r) = -\lambda\exp\{-v(r)\} \quad \text{for } 0 \leq x \leq 1 \tag{71}$$

$$v'(1) = -\frac{\lambda}{|S_3|}, \qquad v'(0) = 0,$$

where $S_3 = \partial B_3$, where $B_3$ is the unit ball of radius 1. The relation between solutions $u(r)$ and $v(r)$ is expressed by the shift

$$v(x) = u(x) + \beta, \tag{72}$$

where the constant $\beta$ is computed from the compatibility and the boundary condition of (71):

$$\lambda = -\oint_{\partial B_3} \frac{\partial v(\boldsymbol{x})}{\partial n}dS = -\lambda\int_{B_3}\exp\{-v(\boldsymbol{x})\}d\boldsymbol{x}, \tag{73}$$

leading to

$$\int_{B_3}\exp\{-v(\boldsymbol{x})\}d\boldsymbol{x} = 1. \tag{74}$$

We obtain from relations (72) and (74),

$$\beta = \log I_\lambda, \tag{75}$$

where $I_\lambda$ is defined for the three dimensions as $I_\lambda = \int_0^1 e^{-u_\lambda(r)} 4\pi r^2\,dr$. The condition $u(0) = 0$ in (13) links the value of $\beta$ to the solution $v(r)$:

$$\beta = v(0). \tag{76}$$

In summary, the solution $u(r)$ can be entirely computed from $v(r)$ as

$$u(r) = v(r) - v(0). \tag{77}$$

The shift in relation (72) permits to express the solution of a nonlinear elliptic PDE, containing the integral of the solution over the domain in terms of the solution of a classical Neumann problem Eq. (71).

We have solved numerically (71) by the one-dimensional finite elements method in Matlab and Comsol for comparison. For the application to the different physical scenarios of PNP in a ball, we used adaptive meshing to account for the stiff tangent in the region close to the boundary $r = R$. For example, for $R = 1\,\mu m$, the maximal element size taken was $5 \cdot 10^{-4}\,\mu m$. All numerical results in the ball $B_3$ (Figs. 4, 3, 6, 7) were obtained using the scheme described here.

## Appendix B. Basic biological terminology

- Dendritic spine: neuronal microstructure located on neuronal cells. It is one of the two part of a synapse, which is a junction between two neurons. The spine geometry is approximated as a spherical head connected to a cylindrical neck see [27].
- PNP: Poisson–Nernst–Planck equation.
- NET: Narrow escape time: mean time for a small particle to find a small hole.
- Voltage-clamp: condition under which the voltage is maintained constant.

## References

[1] I. Rubinstein, Electro-Diffusion of Ions, in: Studies in Applied and Numerical Mathematics, SIAM Publications, Philadelphia, ISBN: 978-0-89871-245-2, 1990.

[2] Z. Schuss, B. Nadler, R.S. Eisenberg, Derivation of Poisson and Nernst-Planck equations in a bath and channel from a molecular model, Phys. Rev. E (3) 64 (2001) 036116.

[3] B. Nadler, Z. Schuss, A. Singer, R.S. Eisenberg, Ionic diffusion through confined geometries: from Langevin to partial differential equations, J. Phys.: Condens. Matter. 16 (2004) S2153–S2165.

[4] D.E. Goldman, Potential, impedance, and rectification in membranes, J. Gen. Physiol. 27 (1) (1943) 37–60.

[5] V. Barcilon, Ion flow through narrow membrane channels: Part I, SIAM J. Appl. Math. 52 (5) (1992) 1391–1404.

[6] V. Barcilon, D.P. Chen, R.S. Eisenberg, Ion flow through narrow membrane channels: Part II, SIAM J. Appl. Math. 52 (5) (1992) 1405–1425.

[7] A. Singer, J. Norbury, A Poisson-Nernst-Planck model for biological ion channelsan asymptotic analysis in a three-dimensional narrow funnel, SIAM J. Appl. Math. 70 (3) (2009) 949–968.

[8] P. Graf, A. Nitzan, M.G. Kurnikova, R. Coalson, A dynamic lattice Monte Carlo model of ion transport in inhomogeneous dielectric environments: Method and implementation, J. Phys. Chem. B 104 (2000) 12324–12338.

[9] A. Taflia, Diffusion of interacting particles in confined domains and applications to biology Weizmann Institute, 2008.

[10] D.A. Frank-Kamenetskii, Diffusion and Heat Exchange in Chemical Kinetics, Princeton Univ. Press, Princeton, NJ, 1955.

[11] G. Wolansky, On steady distributions of self-attracting clusters under friction and fluctuations, Arch. Ration. Mech. Anal. 119 (4) (1992) 355–391.

[12] M. Chipot, I. Shafrir, G. Wolansky, On the solutions of Liouville systems, J. Differential Equations 140 (1) (1997) 59–105.

[13] P. Biler, T. Nadzieja, Existence and nonexistence of solutions for a model of gravitational interaction of particles, I, Colloq. Math. 66 (2) (1994) 319–334.

[14] P. Biler, D. Hilhorst, T. Nadzieja, Existence and nonexistence of solutions for a model of gravitational interaction of particles, II, Colloq. Math. 67 (2) (1994) 297–308.

[15] P. Biler, T. Nadzieja, Global and exploding solutions in a model of self-gravitating systems, Rep. Math. Phys. 52 (2) (2003) 205–225.

[16] D. Holcman, Z. Schuss, Diffusion laws in dendritic spines, J. Math. Neurosci. 1 (10) (2011) 1–14.

[17] D. Holcman, Z. Schuss, Stochatic Narrow Escape. Theory and Applications, Springer, NY, 2015.

[18] R. Araya, V. Nikolenko, K.B. Eisenthal, R. Yuste, Sodium channels amplify spine potentials, Proc. Natl. Acad. Sci. USA 104 (30) (2007) 12347–12352.

[19] R. Araya, K.B. Eisenthal, R. Yuste, Dendritic spines linearize the summation of excitatory potentials, Proc. Natl. Acad. Sci. USA 103 (49) (2006) 18799–18804.

[20] R. Araya, J. Jiang, K.B. Eisenthal, R. Yuste, The spine neck filters membrane potentials, Proc. Natl. Acad. Sci. USA 103 (47) (2006) 17961–17966.

[21] D. Holcman, R. Yuste, The new nanophysiology: how electrodiffusion and geometry regulate ionic flow in neuronal subcompartments, Nat. Rev. Neurosci. (2015).

[22] Z. Schuss, A. Singer, D. Holcman, The narrow escape problem for diffusion in cellular microdomains, Proc. Natl. Acad. Sci. USA 104 (41) (2007) 160981–161103.

[23] D. Holcman, Z. Schuss, Time scale of diffusion in molecular and cellular biology, J. Phys. A 47 (17) (2014) 173001.

[24] J. Jacobsen, K. Schmitt, The Liouville Bratu Gelfand Problem for radial operators, J. Differential Equations 184 (2002) 283–298.

[25] Z. Schuss, Theory and Applications of Stochastic Processes, in: Springer Series in Applied Mathematical Sciences, vol. 170, Springer Verlag, NY, 2010.

[26] K. Tsaneva-Atanasova, A. Burgo, T. Galli, D. Holcman, Quantifying neurite growth mediated by interactions among secretory vesicles, microtubules, and actin networks, Biophys. J. 96 (3) (2009) 840–857.

[27] D. Holcman, Z. Schuss, Modeling calcium dynamics in dendritic spines, SIAM J. Appl. Math. 65 (3) (2005) 1006–1026.

[28] A. Biess, E. Korkotian, D. Holcman, Diffusion in a dendritic spine: the role of geometry, Phys. Rev. E (3) 76 (2007) 021922.

[29] A.F. Cheviakov, M.J. Ward, Optimizing the principal eigenvalue of the Laplacian in a sphere with interior traps, Math. Comput. Modelling 53 (7–8) (2011) 1394–1409.

[30] A. Singer, Z. Schuss, D. Holcman, NARROW ESCAPE, part III: Non-smooth domains and Riemann surfaces, J. Stat. Phys. 122 (3) (2006) 491–509.

[31] E. Korkotian, D. Holcman, M. Segal, Dynamic regulation of spine-dendrite coupling in cultured hippocampal neurons, Eur. J. Neurosci. 20 (10) (2004) 2649–2663.

[32] K. Svoboda, D.W. Tank, W. Denk, Direct measurement of coupling between dendritic spines and shafts, Science 272 (5262) (1996) 716–719.

[33] B.L. Bloodgood, B.L. Sabatini, Neuronal activity regulates diffusion across the neck of dendritic spines, Science 310 (5749) (2005) 866–869.

[34] C. Koch, T. Poggio, A theoretical analysis of electrical properties of spines, Proc. R. Soc. Lond. Ser. B: Biol. Sci. 218 (1213) (1983) 455–477.

[35] I. Segev, W. Rall, Computational study of an excitable dendritic spine, J. Neurophysiol. 60 (2) (1988) 499–523.